The effect of 3d-electron configuration entropy on the temperature coefficient of redox potential in Co1−zMnz Prussian blue analogues

著者（英）	Hiroki Iwaizumi, Yusuke Fujiwara, Yuya Fukuzumi, Yutaka MORITOMO
journal or publication title	Dalton transactions
volume	48
number	6
page range	1964-1968
year	2019-02
権利	(C) The Royal Society of Chemistry 2019
URL	http://hdl.handle.net/2241/00157151

doi: 10.1039/C8DT04338H

Role of 3*d*-electron configuration entropy on temperature coefficient of redox potential in $Co_{1-z}Mn_z$ Prussian blue analogues†

Hiroki Iwaizumi[a], Yusuke Fujiwara[a], Yuya Fukuzumi[a] and Yutaka Moritomo*[a,b,c]

Received Xth XXXXXXXXXX 20XX, Accepted Xth XXXXXXXXX 20XX

First published on the web Xth XXXXXXXXXX 200X

DOI: 10.1039/b000000x

Recently, it was reported that a thermocell can convert temperature into electric energy by using the difference in the thermal coefficient ($\alpha \equiv dV/dT$) of the redox potential (V) between the cathode and anode materials. Here, we systematically investigated α of $Na_xCo_{1-z}Mn_z[Fe(CN)_6]_y$ ($Co_{1-z}Mn_z$-PBA) against Mn concentration (z). The z-dependence of α is interpreted in terms of the 3*d*-electron configuration entropy (ΔS_{3d}) of the redox site. Utilization of S_{3d} is a strategy effective for the design of high-$|\alpha|$ material for energy harvesting thermocell.

A new energy harvesting technology, that converts waste heat near room temperature and/or human body heat to electric energy at low cost and high efficiency, is required for a "smart" society. Recently, several researchers[2–6] reported that a thermocell that uses the difference in the thermal coefficient ($\alpha = dV/dT$) of the redox potential (V) between the anode (α_{anode}) and cathode ($\alpha_{cathode}$) materials can convert the cell temperature (T_{cell}) into the electric energy. The thermocell can produce electric energy in the thermal cycle between low (T_L) and high (T_H) temperatures, making in sharp contract with the semiconductor-based thermoelectric device.[1] In the warming process, the redox potentials of the anode and cathode change by $\alpha_{anode}\Delta T$ and $\alpha_{cathode}\Delta T$, respectively. Then, we expect a thermally induced change in the cell voltage (V_{cell}) as large as $(\alpha_{cathode} - \alpha_{anode})\Delta T$. In other words, electric energy is thermally stored in the thermocell. The stored electric energy can be extracted by the discharge process at T_H. Similarly, during the cooling process, the redox potentials of the anode and cathode change by - $\alpha_{anode}\Delta T$ and - $\alpha_{cathode}\Delta T$, respectively. The stored electric energy can be extracted by the discharge process at T_L. For example, Shibata *et al.*[5] fabricated a thermocell, consisting of two types of cobalt Prussian blue analogues (Co-PBAs) with different α values. The thermocell produces electric energy with high thermal efficiency (η = 1 %) between T_L (= 295 K) and T_H (= 323 K). This type of thermocell expands the application region of the battery materials from energy storage to energy conversion. To realize a new energy harvesting device, exploration of high-$|\alpha|$ is indispensable.

Prussian blue analogues (PBAs) with chemical formula of $Na_xM[Fe(CN)_6]_y$ (M = Fe, Co, Mn and Ni) are promising cathode materials of sodium-ion secondary batteries.[7–14] The compounds consist of three-dimensional (3D) jungle-gym-type host framework with guest Na^+ ions and H_2O molecules, which are accommodated in the nanopores of the framework. Most of the PBAs have face-centered cubic ($Fm\underline{3}m$; Z = 4) or trigonal ($R\underline{3}m$; Z = 3) structures.[15] Importantly, PBAs are also promising materials for the energy harvesting thermocell, because their α values distribute from - 0.3 mVK^{-1} in $Na_xMn[Fe(CN)_6]_{0.83}$ (NMF83) to approximately 1.4 mVK^{-1} in $Na_xCo[Fe(CN)_6]_{0.9}$ (NCF90).[6] Nevertheless, the origin of the wide distribution of α is still unclear. From an thermodynamically point of view, α is equivalent to $\frac{1}{e}\Delta S$, where e and ΔS are the elementary charge (> 0) and the differences in entropy (S) of the system before and after Na^+ insertion. Furthermore, ΔS can be divided into the components due to electrode solid material (ΔS_{solid}) and electrolyte ($\Delta S_{electrolyte}$).[16,17]

In this paper, we investigated α of $Na_xCo_{1-z}Mn_z[Fe(CN)_6]_y$ ($Co_{1-z}Mn_z$-PBA) against Mn concentration (z). We found that $\alpha(z) \approx \alpha(0)$ [$\alpha(0)$ and $\alpha(z)$ are the temperature coefficients of redox potential of NCF90 and $Co_{1-z}Mn_z$-PBA, respectively] in the Co/Mn redox region ($z \leq 0.7$) while $\alpha(z) \ll \alpha(0)$ in the Fe redox region ($z \geq 0.7$). We semi-quantitatively explain the redox site dependence of $\alpha(z)$ in terms of variation (ΔS_{3d}) of the 3*d*-electron configuration entropy (S_{3d}) between the divalent and trivalent states.

Films of $Co_{1-z}Mn_z$-PBA were fabricated by the electrochemical deposition on an indium tin oxide (ITO) transparent electrodes under potentiostatic conditions at - 0.45 V vs. a standard Ag/AgCl electrode.[18,20] The electrolytes

† Electronic Supplementary Information (ESI) available: [details of any supplementary information available should be included here]. See DOI: 10.1039/b000000x/

[a] *Graduate School of Pure & Applied Science, University of Tsukuba, Tennodai 1-1-1, Tsukuba, Ibaraki 305-7571, Japan. E-mail: moritomo.yutaka.gf@u.tsukba.ac.jp*

[b] *Faculty of Pure & Applied Science, University of Tsukuba, Tennodai 1-1-1, Tsukuba, Ibaraki 305-7571, Japan.*

[c] *Tsukuba Research Center for Energy Materials Science (TREMS), University of Tsukuba, Tsukuba, Ibaraki 305-8571, Japan*

Table 1: Chemical formula and concentrations (mmol/L) of the solutes

z	chemical formula	$CoCl_2$	$MnCl_2$	$K_3[Fe(CN)_6]$	NaCl	$Co(NO_3)_2$	$NaNO_3$
0.00	$Na_{1.60}Co[Fe(CN)_6]_{0.90}2.9H_2O$	—	0.00	0.80	—	0.50	5000
0.36	$Na_{1.64}Co_{0.64}Mn_{0.36}[Fe(CN)_6]_{0.91}2.0H_2O$	0.43	0.23	1.00	5000	—	—
0.56	$Na_{1.60}Co_{0.44}Mn_{0.56}[Fe(CN)_6]_{0.90}3.2H_2O$	0.38	0.38	1.00	5000	—	—
0.78	$Na_{1.68}Co_{0.22}Mn_{0.78}[Fe(CN)_6]_{0.92}3.2H_2O$	0.25	0.75	1.00	5000	—	—
0.89	$Na_{1.56}Co_{0.11}Mn_{0.89}[Fe(CN)_6]_{0.89}3.1H_2O$	0.13	1.13	1.00	5000	—	—
1.00	$Na_{1.72}Mn[Fe(CN)_6]_{0.93}2.3H_2O$	0.00	1.50	1.00	5000	—	—

were aqueous solutions containing $K_3[Fe^{III}(CN)_6]$, $Co^{II}Cl_2$ [$Co^{II}(NO_3)_2$], $Mn^{II}Cl_2$, and NaCl ($NaNO_3$). In this process, the reduction reaction of $[Fe^{3+}(CN)_6] + e^- \rightarrow [Fe^{2+}(CN)_6]$ triggers the deposition of PBA. Therefore, Fe, Mn, and Co in the as-grown films are divalent. The chemical composition of the film can be finely controlled by the concentration of the solutes (Table 1). For example, the z value can be controlled by the concentrations ratio between Co^{2+} and Mn^{2+}. Chemical compositions of the films were determined using the inductively coupled plasma (ICP) method and are listed in Table 1. The obtained film was transparent (Fig. S1) with a thickness of $\approx 1\ \mu$m . In the whole region of z, the crystal structure of the as-grown film was hexagonal (Fig. S2). The lattice constants, a and c, monotonously increase with z (Fig. S3), reflecting the larger ionic radius ($r_{Mn^{2+}}$ = 0.830 Å) of Mn^{2+} as compared with that ($r_{Co^{2+}}$ = 0.745 Å) of Co^{2+}.

The electrochemical measurements were carried out with a potentiostat (HokutoDENKO HJ1001SD8) in an Ar-filled glove box using a beaker-type cell. The cathode, anode, and electrolyte were the film, Na metal, and propylene carbonate (PC) containing 1 mol/L $NaClO_4$, respectively. The charge and discharge rate were about 1 C. The cut-off voltage was from 2.8 to 4.0 V. The x value in $Co_{1-z}Mn_z$-PBA was evaluated from the total current under the assumption that x = 0.0 in the charged state.

Figure 1 shows discharge curves of the $Co_{1-z}Mn_z$-PBA films; (a) z = 0.0, (b) 0.56, (c) 0.89, and (d) 1.00. In whole the region of z, the discharge curves show two-plateau feature. At z = 0.0 [(a)], the high- and low-V plateaus are observed around 3.8 and 3.3 V, respectively. The high-V plateau is ascribed to the redox reaction of Fe^{2+}/Fe^{3+}, while the low-V plateau is ascribed to the redox reaction of Co^{2+}/Co^{3+}.[21] At z = 1.0 [(d)], the high- and low-V plateaus are observed around 3.6 and 3.4 V, respectively. The high-V plateau is ascribed to the redox reaction of Mn^{2+}/Mn^{3+}, while the low-V plateau is ascribed to the redox reaction of Fe^{2+}/Fe^{3+}.[21] We note that the redox site at the low-V plateau switches from Co (z = 0.0) to Fe (z = 1.0).

At the boundary between the high- and low-V plateaus, the electronic configuration of the low- and high-z samples are Co^{3+} (Mn^{3+}) - Fe^{2+} and Mn^{2+} (Co^{2+}) - Fe^{3+}, respectively. We note that ionic radii of Co^{2+} ($r_{Co^{2+}}$ = 0.745 Å) and Mn^{2+}

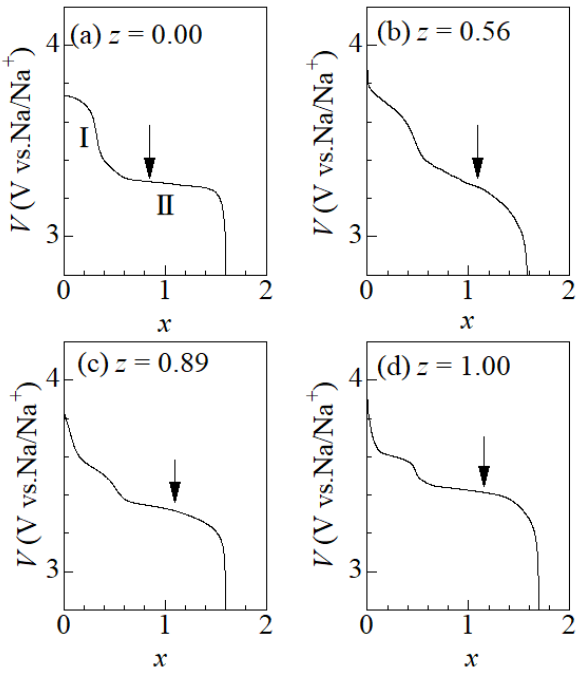

Fig. 1: Discharge curves of the $Co_{1-z}Mn_z$-PBA films; (a) z = 0.0, (b) 0.56, (c) 0.89, and (d) 1.00. The discharge rate was about 1 C. Arrows represent the x value of the films used in the test cell (see text).

($r_{Mn^{2+}}$ = 0.830 Å) are much larger than those of the other ions. Then, we may expect discontinuous increase of the lattice constant at the switching of the redox site from Co (Mn) to Fe. We investigated the crystal structure of the x-controlled $Co_{1-z}Mn_z$-PBA at the boundary bwetwwn the high- and low-V plateaus. In the whole region of z, the crystal structure was face-centered cubic (Fig. 4S). As expected, the lattice constant (a) shows discontinuously jumps at $z \approx 0.7$ from a = 10.09 Å to 10.41 Å (Fig. 5S). Here, let us evaluate the variation (Δa) of a by the change of the ionic radii. The change of the ionic radii of Co, Mn and Fe are Δr_{Co} = 0.20 Å, Δr_{Mn} = 0.185 Å and Δr_{Fe} = - 0.06 Å, respectively. Then, Δa [= $0.3\Delta r_{Co}$ + $0.7\Delta r_{Mn}$ + Δr_{Fe}] becomes 0.38 Å, which is close to the experimental value (= 0.32 Å). In addition, the color of the film at the

Table 2: Chemical composition of $Na_xCo_{1-z}Mn_z[Fe(CN)_6]_y$ that is used as anode and cathode of the test cell. $\alpha_{cathode}$ and α_{anode} are the temperature coefficients of redox potential of cathode and anode, respectively.

annode			cathode			
z	y	x	z	y	x	$\alpha_{cathode}$ - α_{anode} (mVK^{-1})
0	0.90	0.81	0.36	0.91	0.94	- 0.38
0	0.90	0.91	0.56	0.90	1.09	- 0.32
0	0.90	0.96	0.78	0.92	1.07	- 0.89
0	0.90	0.97	0.89	0.89	1.00	- 1.50
0	0,90	0.91	1.00	0.93	1.15	- 1.75

middle point of the low-V plateau significantly changes from deep purple at z = 0.56 to reddish brown at 0.78 (Fig. S1). The deep purple color is ascribed to the electronic transition from Fe^{2+} to Co^{3+}.[19] Then, the switching of the redox site causes the significant color change as observed, because the Co state changes from trivalent to divalent. A similar switching of the redox site was reported by Kurihara *et al.*[20] in the isomorphic lithium compound ($Li_xCo_{1-z}Mn_z[Fe(CN)_6]_y$), in which the redox site at the low-V plateau changes from Co/Mn ($z \leq$ 0.7) to Fe ($z \geq 0.7$).

Recently, Fukuzumi *et al.*[6] reported that α = 1.4 mV/K in the low-V plateau of $Na_xCo[Fe(CN)_6]_{0.9}$ (NCF90). Therefore, we regarded the NCF90 (z = 0.0) film as a standard of α. We fabricated a low-V_{cell} cell whose anode, cathode and electrolyte were the NCF90 film, $Co_{1-z}Mn_z$-PBA films, and PC containing 1 mol/L $NaClO_4$, respectively. The areas of the electrodes are $\approx$ 1.0 cm^2. To avoid the potential fluctuation effect which is significant in the as-grown (fully-reduced) state, x of the NCF90 and $Co_{1-z}Mn_z$-PBA films were controlled to the middle point of the low-V plateau (arrows in Fig. 1) using a beaker-type cell. The chemical composition of the anode and cathode of the thermocell are summarized in Table 2. In the high-V plateau, the redox potential was too unstable agasint time to determine reliable α. We carefully measured V_{cell} of the NCF90/$Co_{1-z}Mn_z$-PBA cell (test cell) against T_{cell}. T_{cell} was monitored with a Pt resistance thermometer in the electrolyte and was slowly increased/decreased at a rate of $\approx \pm$ 0.3 K/min.

Figure 2 shows V_{cell} of the test cell against T_{cell}; (a) z = 0.36, (b) 0.56, (c) 0.89, and (d) 1.00. Red and blue marks mean that the data obtained in the heating and cooling runs, respectively. We observed no thermal hysteresis of V_{cell}, indicating that the data are free from temperature gradient nor sample deterioration effects. $\Delta\alpha$ [= $\alpha(z)$ - $\alpha(0)$] was evaluated by least-squares fittings. In the small-z region [(a) and (b)], $|\Delta\alpha|$ is small ($\leq$ 0.32 mVK^{-1}) indicating that $\alpha(z) \approx \alpha(0)$ (= 1.4 mVK^{-1}). In the large-z region [(c) and (d)], $|\Delta\alpha|$ is large ($\geq$ 1.50 mVK^{-1}) indicating that $\alpha(z) \ll \alpha(0)$. Figure 3(a) shows thus determined $\alpha(z)$ [= $\Delta\alpha$ + $\alpha(0)$] against z. In the low-z region ($z \leq$

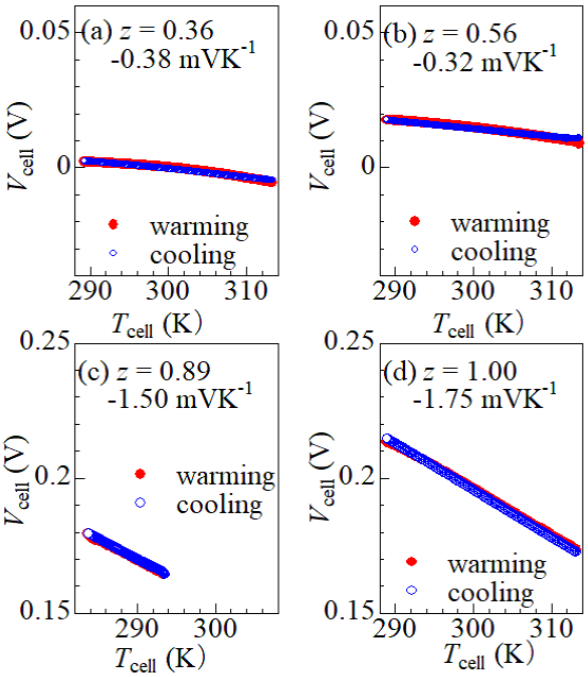

Fig. 2: Cell voltage (V_{cell}) of the NCF90/$Co_{1-z}Mn_z$-PBA cell against the cell temperature (T_{cell}); (a) z = 0.36, (b) 0.56, (c) 0.89, and (d) 1.00. Both the anode and cathode were the x-controlled films to the middle point of the low-V plateau. Red and blue marks mean that the data obtained in the healing and cooling runs, respectively.

0.7), $\alpha(z)$ is almost the same as $\alpha(0)$ (= 1.4 mVK^{-1}). In the large-z region ($z \geq 0.7$), $\alpha(z)$ steeply decreases and finally becomes negative (= - 0.1 - - 0.4 mVK^{-1}) above z = 0.89. The negative $\alpha(z)$ in the large-z region is consistent with the negative value in $Na_xMn[Fe(CN)_6]_{0.83}$ (NMF83).[6] Thus, we confirmed that the magnitude of $\alpha(z)$ has strong correlation with the redox site. $\alpha(z)$ is large in the Co/Mn redox region ($\leq$ 0.7) while $\alpha(z)$ is small in the Fe redox region ($\geq$ 0.7).

Figure 3(b) shows V_{cell} (= V_z - V_0, where V_0 and V_z is the redox potential of NCF90 and $Co_{1-z}Mn_z$-PBA, respectively) of the test cell at 290 K. In the small-z region ($z \leq 0.7$), V_{cell} is nearly zero indicating that $V_z \approx V_0$. At $z \approx 0.7$, V_z discontinuously jumps from V_{cell} = 20 mV at z = 0.56 to 125 mV at 0.78. With further increase in z, α steeply increase to from V_{cell} = 125 mV at z = 0.78 to 213 mV at z = 1.00. This discontinuous jump of V_z at z = 0.7 is probably ascribed to the redox site switching from Co/Mn ($z \leq 0.7$) to Fe ($z \geq 0.7$).

Now, let us consider the effect of the 3d-electron configuration entropy (S_{3d}) on α. From a thermodynamically point of view, α is equivalent to $\frac{1}{e}\Delta S$. Then, the contribution of S_{3d} on α is expressed as $\frac{1}{e}\Delta S_{3d} = \frac{1}{e}(S_{3d}^{di} - S_{3d}^{tri})$, where S_{3d}^{di} and S_{3d}^{tri} are the configuration entropy in the divalent and trivalent states, respectively. S_{3d} is expressed as $k_B \ln W$, where W (= N_{spin} $\times$

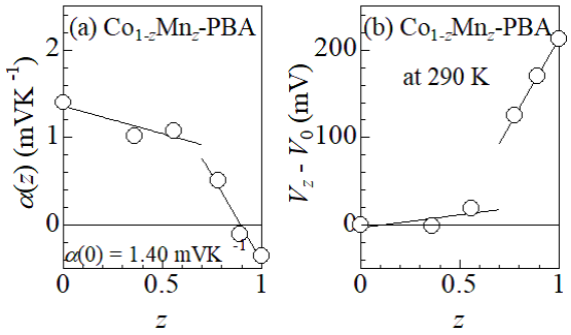

Fig. 3: (a) Thermal coefficient [α(*z*)] of redox potential in $Co_{1-z}Mn_z$-PBA against *z*. (b) V_{cell} (= V_z - V_0, where V_0 and V_z is the redox potential of NCF90 and $Co_{1-z}Mn_z$-PBA, respectively) of the NCF90/$Co_{1-z}Mn_z$-PBA cell against *z* at 290 K. Both the anode and cathode were the *x*-controlled films to the middle point of the low-*V* plateau. The straight lines are merely guides to the eyes.

$N_{orbital}$, where N_{spin} and $N_{orbital}$ are spin and orbital degrees of freedom, respectively) is the number of degenerated electronic configuration. In Table 3, we summarize S_{3d}^{di} and S_{3d}^{tri} of Co, Mn, and Fe, together with the numerical evaluation of $\frac{1}{e}\Delta S_{3d}$. N_{spin} is expressed as $2S + 1$, where S is the total spin quantum number. $N_{orbital} = 3$ in the $e_g^2t_{2g}^5$ and $e_g^0t_{2g}^5$ configurations, because we can select three orbitals for the t_{2g} hole. $N_{orbital} = 2$ in the $e_g^1t_{2g}^3$ configuration, because we can select two orbitals for the e_g electron. $N_{orbital} = 1$ in the $e_g^0t_{2g}^6$ and $e_g^2t_{2g}^3$ configurations, because there is no degenerated configuration. In PBAs, the oxidization process of Co^{2+} causes spin state transition from high-spin (Co^{2+}) to low-spin (Co^{3+}) states. The redox process of Co^{2+}/Co^{3+} contributes to α(*z*) by 0.21 mVK^{-1} while that of Fe^{2+}/Fe^{3+} contributes to α(*z*) by - 0.15 mVK^{-1}. Thus, ΔS_{3d} semi-quantitatively explains why α (= 1.40 mVK^{-1}) in Co-PBA is larger than that (= - 0.35 mVK^{-1}) in Mn-PBA. In other words, the high α value of NCF90 is ascribed to the spin state transition of the Co ion accompanied by the redox reaction. The observed difference (= 1.75 mVK^{-1}) in α between Co-PBA and Mn-PBA, however, is larger than the difference (= 0.36 mVK^{-1}) evaluated based on ΔS_{3d}. This implies that another effects, *e.g.*, variation of the vibrational mode around the redox site, contribute to ΔS_{solid}.

Finally, let us briefly comment on how to enhance the thermal efficiency (η). The electronic energy extracted from the thermocell is expressed as $Q \times V_{cell}$, where Q is the extracted charge. Then, η increases with increase in V_{cell} and/or Q. Above discussion on S_{3d} gives us a strategy how to increase V_{cell} [= $\Delta\alpha(T_H - T_L)$]. Looking at Table 2, one may notice that Δα becomes large if Co^{2+}/Co^{3+} and Fe^{2+}/Fe^{3+} redox materials are used as cathode and anode, respectively. Actually, the high-η value (= 1%) reported in the thermocell consists of two types of Co-PBAs[5] can be reinterpreted in terms of the ΔS_{3d} scenario. On the other hand, Shibata *et al.*[22] reported that the magnitude of Q is quantitatively reproduced by the slopes of the discharge curves. This indicates that Q is expected be larger in the material whose discharge curve is flatter.

Table 3: 3*d*-electron configuration entropy (S_{3d})

ion	electron configuration	S_{3d}	$\frac{1}{e}\Delta S_{3d}$
Co^{2+}	$e_g^2t_{2g}^5$	$k_B\ln(4\times3)$	—
Co^{3+}	$e_g^0t_{2g}^6$	$k_B\ln(1\times1)$	—
—	—	—	0.21 mVK^{-1}
Mn^{2+}	$e_g^2t_{2g}^3$	$k_B\ln(6\times1)$	—
Mn^{3+}	$e_g^1t_{2g}^3$	$k_B\ln(5\times2)$	—
—	—	—	- 0.04 mVK^{-1}
Fe^{2+}	$e_g^0t_{2g}^6$	$k_B\ln(1\times1)$	—
Fe^{3+}	$e_g^0t_{2g}^5$	$k_B\ln(2\times3)$	—
—	—	—	- 0.15 mVK^{-1}

In conclusion, we systematically investigated α(*z*) in $Co_{1-z}Mn_z$-PBA against *z*. We found that $\alpha(z) \approx \alpha(0)$ in the Co/Mn redox region ($z \leq 0.7$) while $\alpha(z) \ll \alpha(0)$ in the Fe redox region ($z \geq 0.7$). We semi-quantitatively explain the redox site dependence on α(*z*) in terms of the 3*d*-electron configuration entropy (S_{3d}). Utilization of S_{3d} is a strategy effective for the design of high-|α| material for energy harvesting thermocell.

This work was supported by JSPS KAKENHI (Grant Number JP17H0113). The synchrotron radiation experiments were performed at the BL02B2 of SPring-8 with the approval of the Japan Synchrotron Radiation Research Institute (JASRI) (Proposal No. 2018A1125 and 2017A1040). The elementary analyses were performed at the Chemical Analysis Division, Research Facility Center for Science and Engineering, University of Tsukuba.

Conflicts of interest

There are no conflicts of interest to declare.

References

1 H. J. Goldsmid, Introduction to Thermoelectricity, Springer-Verlag, Berlin, 2010.
2 S. W. Lee, Y. Yang, Y.-H. Lee, H. Ghasemi, D. Kraemer, G. Chen. and Y. Cui. Nat. Commun. 2014, **5**, 3942.
3 Y. Yang, S. W. Lee, H. Ghasemi, J. Loomis, X. Li, D. Kraemer, G. Zheng, Y. Cui, and G. Chen, PNAS, 2014, **111**, 17011-17116.
4 J. Wang, S.-P. Feng, Y. Yang, N. Y. Hu, M. Munro, E. Ferreira-Yang, and G. Chen, Nano Lett. 2015, **15**, 5784-5790.
5 T. Shibata, Y. Fukuzumi, W. Kobayashi, and Y. Moritomo, Appl. Phys. Express, 2018, **11**, 017101.
6 Y. Fukuzumi, K. Amaha, W. Kobayashi, H. Niwa, and Y. Moritomo, Energy Technol., 2018, **6**, 1-7.

7 Y. Lu, L. Wang, J. Cheng, and J. B. Goodenough, Chem. Commun., 2012, **48**, 6544 - 6546.

8 T. Matsuda, M. Takachi, and Y. Moritomo, Chem. Commun., 2013, **49**, 2750-2752.

9 M. Takachi, T. Matsuda, and Y. Moritomo, Appl. Phys. Express, 2013, **6**, 025802.

10 D. Yang, J. Xu, X.-Z. Liao, Y.-S. He, H. Liu, and Z.-F. Ma, Chem. Commum., 2014, **50**, 13377-13380.

11 H. W. Lee, R. Y. Wang, M. Pasta, S. W. Lee, N. Liu, and Y. Chi, Nat. Commun., 2014, **5**, 5280.

12 L. Wang, J. Song, R. Q. Qiao, L. A. Wray, M. A. Hossain, Y.-D. Chung, W. Yang, Y. Lu, D. Evans, J.-J. Lee, S. Vail, X. Zhao, M. Nishijima, S. Kakimoto, and J. B. Goodenenough, J. Am. Chem. Soc., 2015, **137**, 2548-2554.

13 S. Yu, Y. Li, Y. Lu, B. Xu, Q. Wang, M. Yan, and Y. A. Jiang, Y., J. Power Sources, 2015, **275**, 45-49.

14 Y. You, X.-L. Wu, Y.-X. Yin, and Y.-G. Guo, Energy Environ. Sci.,2014, **7** 1643-1647.

15 H. Niwa, W. Kobayashi, T. Shibata, H. Nitani, and Y. Moritomo, Sci. Reps. 2017, **7**, 13225.

16 Y. Fukuzumi, Y. Hinuma, and Y. Moritomo, J. Phys. Soc. Jpn., 2018, **87**, 055001.

17 Y. Fukuzumi, Y. Hinuma, and Y. Moritomo, AIP Adv., 2018, **6**, 065021.

18 K. Igarashi, F. Nakada, and Y. Moritomo, Phys. Rev. B, 2008, **78**, 235106.

19 Y. Kurihara, H. Funashima, M. Ishida, N. Hamada, T. Matsuda, K. Igarashi, H. Tanida, T. Uruga, and Y. Moritomo, J. Phys. Soc. Jpn., 2010, **79**, 044710.

20 Y. Kurihara and Y, Moritomo, Jpn. J. Appl. Phys. 2014, **53**, 067101.

21 M. Takachi, T. Matsuda, and Y. Moritomo, Jpn. J. Appl. Phys. Appl. Phys., 2013, **52**, 090202

22 T. Shibata, Y. Fukuzumi, and Y. Moritomo, Sci. Reps., 2018, **8**, 14784.